Research Article Vol. 9, No. 11 | 1 Nov 2018 | BIOMEDICAL OPTICS EXPRESS 5489

Biomedical Optics EXPRESS

Mapping the phase and amplitude of ossicular chain motion using sound-synchronous optical coherence vibrography

ANTOINE RAMIER,[1,2] JEFFREY TAO CHENG,[3] MICHAEL E. RAVICZ,[3] JOHN J. ROSOWSKI,[3] AND SEOK-HYUN YUN[1,2,*]

[1] *Harvard-MIT Division of Health Sciences and Technology, Cambridge, MA, USA*
[2] *Wellman Center for Photomedicine, Massachusetts General Hospital, Boston, MA, USA*
[3] *Eaton-Peabody Laboratories, Massachusetts Eye and Ear Infirmary, Boston, MA, USA*
**syun@mgh.harvard.edu*

Abstract: The sound-driven vibration of the tympanic membrane and ossicular chain of middle-ear bones is fundamental to hearing. Here we show that optical coherence tomography in phase synchrony with a sound stimulus is well suited for volumetric, vibrational imaging of the ossicles and tympanic membrane. This imaging tool — OCT vibrography — provides intuitive motion pictures of the ossicular chain and how they vary with frequency. Using the chinchilla ear as a model, we investigated the vibrational snapshots and phase delays of the manubrium, incus, and stapes over 100 Hz to 15 kHz. The vibrography images reveal a previously undescribed mode of motion of the chinchilla ossicles at high frequencies.

1. Introduction

The tympanic membrane (TM) and ossicular chain play a central role in hearing by providing acoustic impedance matching between the air-filled ear canal and the fluid-filled inner ear. The incoming sound energy is collected by the TM, transmitted through the ossicles to the cochlear fluid, and detected and transformed to neural signals in the inner ear. A dysfunction or damage in the middle ear results in hearing impairment.

Vibrometric measurement of the ossicles and TM has been critical for advancing our understanding of the hearing mechanics and improving treatments such as middle-ear prosthetics. Vibro-acoustic analysis of the middle ear and TM has also been proposed for diagnosis of ossicular disorders and planning surgical interventions [1–3]. In the past, stroboscopic microscopy, capacitive probes, and the Mössbauer effect were used to measure the sound-induced vibrations at specific locations in the middle ear [4,5]. Modern investigations are generally conducted using more sensitive optical interferometric techniques, particularly laser Doppler vibrometry (LDV) and holography [6–8]. LDV and holography are surface measurement techniques and, therefore, require surgical preparation to access structures beyond the TM [9]. They are also subject to artefacts caused by other vibrating structures located behind the tissue of interest if those structures are sufficiently reflective [10].

Optical coherence tomography (OCT) is a cross-sectional imaging modality and its potential for structural imaging of the middle ear has been previously explored [11], primarily for assessing pathologies, such as otitis media [12], middle ear effusions [13], and cholesteatoma [14], in diagnostic and intraoperative settings [15,16]. Beyond anatomical imaging, phase-sensitive OCT has shown a promising potential for vibration measurements in hearing research [17–23]. Subhash *et al.* made one of the first demonstrations of depth-resolved OCT vibrometry at a sound frequency of 500 Hz using a spectrometer-based OCT system [24]. Several groups demonstrated OCT vibrometry of the TM [25–28] and ossicles [29,30] with improved imaging and processing speeds, as well as interfaces suitable for live

#336583 https://doi.org/10.1364/BOE.9.005489
Journal © 2018 Received 2 Jul 2018; revised 10 Sep 2018; accepted 12 Sep 2018; published 17 Oct 2018

patient imaging. Up to now, the demonstrations of OCT-based middle ear vibrometry have been largely focused on vibration magnitude, and vibration phase has been generally overlooked. Measuring the phase of vibration with respect to sound stimuli allows the acoustic phase and group delays to be determined along different middle ear components. Accurate measurements of the relative phase of motion along the ossicular chain can help determine modes of motion and identify differences between normal and pathologic states. We have previously developed a technique, called OCT vibrography, to acquire the magnitude and phase of vibration at each location through successive vibrational cycles and reconstruct effective snapshot images of the TM and ossicular motion. However, the system had a limited frequency range below 3 kHz and suffered from random phase noise drift with respect to the sound source, making it difficult to measure phase delays through the ossicular chain reliably and accurately [31].

In this article, we present an improved OCT system that has overcome these two limitations and demonstrates considerably more precise measurement of the phase delay along the ossicular chain. In chinchilla ears, our results revealed a new mode of vibration, involving twist and bending of the ossicular structure, for acoustic transduction at frequencies above 10 kHz.

2. OCT vibrography system

2.1 Optical system, sound stimulus, and time synchronization

The imaging system (Fig. 1) uses a wavelength-swept laser based on a rotating polygon mirror [32–34]. The laser output has a center wavelength of 1280 nm and a 3-dB bandwidth of 80 nm at a sweep rate of 45 kHz. The corresponding axial resolution is 15 µm. A fiber-based Mach-Zehnder interferometer (MZI) (Thorlabs INT-MZI-1300) is employed to provide reference interference fringes for clock jitter compensation. In the sample arm, the laser beam is scanned by a pair of galvanometer mirror scanners (Cambridge Technology, 6210H), expanded by lenses L1 (50 mm) and L2 (75 mm) and focused by an objective lens L3 (100 mm) to a spot size (lateral resolution) of 30 µm (full width at half maxima) at the focus. The total optical power incident on the sample is 10 mW. Additionally, a long-pass dichroic mirror with a cutoff wavelength of 950 nm is employed and directs room light reflected from the sample to a CCD camera (Allied Vision, Mako G) to provide an otoscopic view of the sample, facilitating sample alignment.

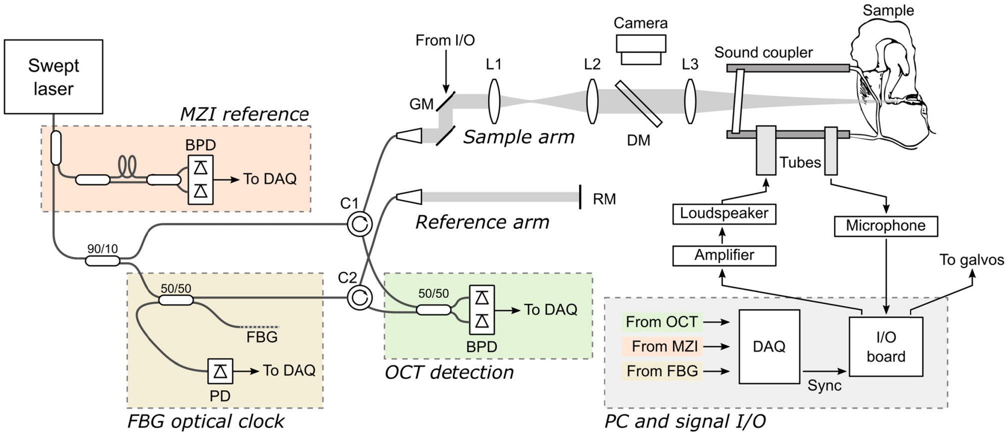

Fig. 1. Schematic of the optical system and signal generation and acquisition. Abbreviations used: Mach-Zehnder interferometer (MZI), photodiode (PD), balanced photodiode (BPD), data acquisition (DAQ) system, fiber Bragg grating (FBG), circulators (C1, C2), galvanometer mirrors (GM), lenses (L1-L3), reference mirror (RM), dichroic mirror (DM).

An all-purpose input/output (I/O) board (National Instrument, USB-6353) is used to generate electrical waveforms to drive a compression speaker (Peavey RX22) via a 300W power amplifier (Crown Audio, XLI). The output face of the speaker is directly coupled to a latex tube connected to a custom-built sound coupling tube made of brass. One side of the brass tube has a transparent, tilted glass window to transmit the optical imaging beam. The other side of the tube is coupled to the auditory canal of the specimen. A low-noise microphone (Etymotic ER-7C) in the coupler records the stimulus sound pressure *in situ* within 5 mm of the center of the TM.

A fiber Bragg grating (FBG) and photodiode (PD) provide a pulse signal synched to each wavelength sweep of the laser output ("FBG optical clock"). This signal triggers a high-speed data acquisition (DAQ) card for digitizing interferometric signals from dual balanced photodetectors (BPD) in the OCT interferometer and the reference MZI. The output trigger of the DAQ card is then used as the clock "Sync" signal for the I/O board that generates the sound stimulus, controls the galvanometer scanners, and acquires the microphone signal. This arrangement ensures time synchronization for the measurement of OCT interference signals, beam scanning, and the generation and recording of sound waves. The timing jitter measured using a digital oscilloscope (Keysight DSO1024A, 200 MHz, 2 GS/s) between the I/O board output and the FBG clock was 5.7 ns, which provides a phase uncertainty of less than 9x10^{-5} cycles with stimuli of 15000 Hz.

2.2 Data acquisition in synchrony with sound frequency

Each complete wavelength (λ) sweep of the laser yields an individual axial scan (A-line) along the depth (z) axis. The optical beam is scanned in the transverse directions (x and y) to form a complete volume image. The A-line rate (f_A) is the same as the wavelength-sweep repetition rate. The digitization rate of the DAQ is set to 99 MHz so that 2,048 samples of the dual-balanced detector signal are acquired during each A-line. For phase synchrony, the acoustic frequency f_s is restricted to be an integer fraction of the A-line rate; that is, $f_s = f_A\, n/m$, where n and m are integers. The data acquisition and beam scanning are arranged such that m A-lines are acquired at every transverse location (an M-scan) during n cycles of the sound wave (Fig. 2). Typically, we set m to be a rather large, even number in a range of 180 to 250, and n is variable from the minimum of 1 for low sound frequencies, up to 100 for high frequencies within the Nyquist criterion. With $m = 200$, for example, for a wavelength sweep rate of 45 kHz, the allowed f_s ranges from 225 Hz (n = 1) to 22.5 kHz ($n = 100$) at an interval of 225 Hz. A different m value yields a different set of f_s. This allows a wide range of sound frequencies to be tested. For $f_A = 45$ kHz and $m = 200$, the acquisition of a single M-scan at each transverse location takes 4.44 ms, regardless of the sound frequency. Data acquisition over an entire frame (128 M-scans) or volume (128 × 128 M-Scans) takes 0.57 s and 72.7 s, respectively. Such sampling produces a 3D data set of vibrography images at one sound frequency of 1024 (z) × 128 (x) × 128 (y) voxels. Such a measurement set is repeated for each sound stimulus frequency.

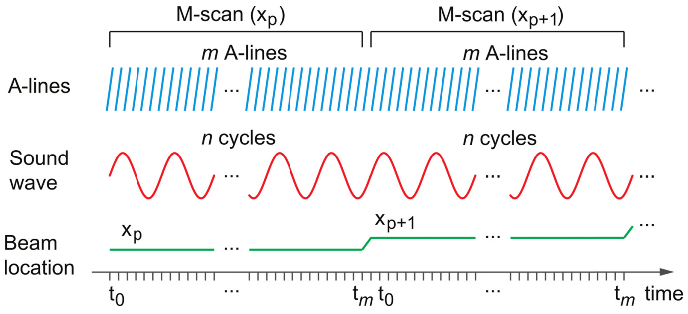

Fig. 2. Timing diagrams of data acquisition, sound wave, and beam position scan.

2.3 Data processing to determine the amplitude and phase of vibration

For each A-line, the wavelength-domain interferogram is corrected for a background offset and resampled linearly in wavenumber (k) based on the MZI reference data [35]. This step also reduces timing jitter between the data acquisition clock and wavelength sweep [36]. The resampled interferogram is multiplied by an apodization window function and further corrected for chromatic dispersion in the interferometer. The corrected interference fringes $a(k,t,x,y)$ are Fourier transformed (k to z) to produce an A-line profile, $A(z,t,x,y)$. The magnitude of the complex A-line represents optical reflectance and is displayed (in log scale) to show the structure of the sample. The phase $\phi(z,t,x,y)$ of the A-line contains the z-axis coordinates of the structure within a sub-wavelength range. It should be noted that the phase ϕ represents the phase of the optical interference signal and should not be confused with a "vibration phase" denoted φ, which refers to the phase of the mechanical motion of the structure. The sinusoidal displacement of each voxel at (z, x, y) at time t, $u_z\left(z,t,x,y\right)=\left|u\right|e^{i(2\pi f_s t+\varphi)}$, is linked to the interference phase OCT via:

$$u_z\left(z,t,x,y\right)=\frac{\lambda_0}{4\pi n_0}\phi\left(z,t,x,y\right) \tag{1}$$

where λ_0 is the center wavelength of the swept source in vacuum, and n_0 is the refractive index of the medium. The optical phase difference $\Delta\phi$ between adjacent A-lines at each spatial location is computed with [37]:

$$\Delta\phi\left(t_i,ROI\right)=\arg\left(\sum_{ROI}A^*\left(z,t_{i-1},x,y\right)A\left(z,t_i,x,y\right)\right) \tag{2}$$

where A^* denotes the complex conjugate of $A(z,t,x,y)$, and the summation is carried over a region of interest (ROI) for averaging motion within the region. The ROI may be a short axial segment or small volume. The averaging enhances the effective sensitivity of phase measurement without affecting spatial resolution because phase does not change significantly over multiple imaging voxels. The ROI-averaged displacement function is given by: $u_z\left(t_k,ROI\right)=\frac{\lambda_0}{4\pi n_0}\sum_{i=1}^{k}\Delta\phi\left(t_i,ROI\right)$, where the summation integrates the phase differences to obtain accumulated absolute phase from t_0, the beginning of each sound wave cycle.

The time series of displacement functions $u_z(t,ROI)$ contains all the information about the axial component of the sound-driven vibration. The magnitude and phase of the mechanical vibration at the sound frequency can be readily obtained by a Fourier transform of the displacement with respect to the time coordinate:

$$U_z\left(f,ROI\right)=\mathcal{F}\left\{u_z(t,ROI)\right\} \tag{3}$$

The amplitude and phase of $U_z(f_s,x,y,z)$ at the applied sound frequency f_s gives the magnitude and phase of vibration in response to the stimulus. The acoustic transfer function is obtained by normalizing the measured signal with respect to the input sound stimulus recorded with the microphone. Axial velocity v_z ($\equiv du_z/dt$) is computed from $(i2\pi f_s)U_z(f_s)$.

The smallest vibration that can be measured is ultimately limited by the optical signal-to-noise ratio (SNR), defined as the power ratio of the amplitude (reflectivity) to the noise floor of $|A(z,x,y)|$. To a first-order approximation, the theoretical limit of vibration sensitivity σ_u is given by [36,38,39]:

$$\sigma_u=\frac{\lambda_0}{4\pi n_0}\frac{1}{\sqrt{\mathrm{SNR}}} \tag{4}$$

Upon taking the Fourier transform (*t* to *f*), the M-scan is effectively averaged *m* times, such that the frequency-domain amplitude sensitivity is $\sigma_{|U|} = \sigma_u / \sqrt{m}$. The theoretical sensitivity can be further improved with ROI averaging (described above) by a factor of $\sqrt{N}$ when the ROI consists of *N* samples with an equal SNR.

The SNR-limited vibration phase noise is linked to the amplitude noise and given by:

$$\sigma_{\varphi} = \frac{\sigma_{|U|}}{|U|} \tag{5}$$

The phase noise is also reduced by a factor of $\sqrt{N}$ when the data are averaged over *N* samples.

At stimulus levels above ~100 dB SPL, the TM can move more than $\lambda_0/2$ between two consecutive A-line scans, making $|\Delta\phi| > \pi$. This can cause a phase wrapping artifact in the phase-sensitive measurement because the phase difference $\Delta\phi$ has 2π ambiguity. In addition, the TM motion can generate erroneous optical phase readings when the amplitude of motion becomes larger than the axial resolution of the OCT system. To avoid these artifacts, we limited the stimulus to levels where these artifacts did not occur. When we concentrate on ossicular motion, the SPL level is varied to produce a full-range of ossicular motion, and care is taken to segment out the TM region causing artifacts.

2.4 System performance measurement: phase sensitivity and stability

To characterize the sensitivity of our OCT vibrography system, we measured the vibration signal from a stationary object (2.8-kg block of aluminum) while varying the SNR by adjusting the optical power in the sample arm using a variable attenuator. First, the galvanometer scanner was turned off, and a 1 s M-scan was acquired for each level of attenuation. Then, another set of M-scans was acquired while the galvanometer scanner was turned on and a constant voltage was applied so that the probe beam was held at a fixed location on the object. The optical SNR, motion amplitude sensitivity, and noise spectra were computed from the data set.

The sensitivity measured with the scanner off was in good agreement with the theoretical limitation (Fig. 3(a)). However, when the scanner was on, we found an excess amplitude noise with an amplitude of 4 nm, which is presumably due to mechanical jitter of the galvanometer mirror coupled with the feedback control of the driver. At relatively high SNR levels above 30 dB, the system's sensitivity was limited by this scanner noise. In most parts of the middle ear structure, the optical SNR tends to be below 30 dB, in which the measurement is SNR-limited. The noise floor without the scanner noise was flat in the frequency domain (Fig. 3(b)) as expected from a purely SNR-limited case. When the scanner was on and the SNR was >35 dB, the mechanical scanner noise described a broad envelope centered around 8 kHz. The noise spectrum without the scanner noise revealed sharp noise peaks with an equal spacing of 625 Hz, which correspond to the 72 facets of the rotating polygon filter in the wavelength-swept laser source. We avoided these fixed noise frequencies when setting the sound stimulus frequency.

Next, to measure vibration phase noise we placed a piezoelectric transducer (PZT) in the sample stage. The transducer was driven to oscillate with an amplitude of ~5 nm at a constant frequency of 9 kHz. Figure 3(c) shows the variation of measured vibration phase relative to the phase of the stimulus over a duration of 1 s, measured synchronized to the stimulus generation as described above ("Sync"). Each data point represents an average of 225 A-lines, a simulation of ROI averaging with $N = 225$ that was used in some middle-ear imaging experiments described later. Apart from some random fluctuation, the measured phase was stable over time. However, when the PZT was driven by a function generator with an independent clock (“Sync Off”), we measured large, random phase drift, confirming the benefit to phase stability of timing synchronization.

To characterize the phase noise, we varied the optical SNR using a variable attenuator in the sample arm of the OCT interferometer. The scanner was turned off to remove the effect of the mechanical noise. The result agreed well with the theoretical line for a SNR-limited case with $N = 225$ (Fig. 3d).

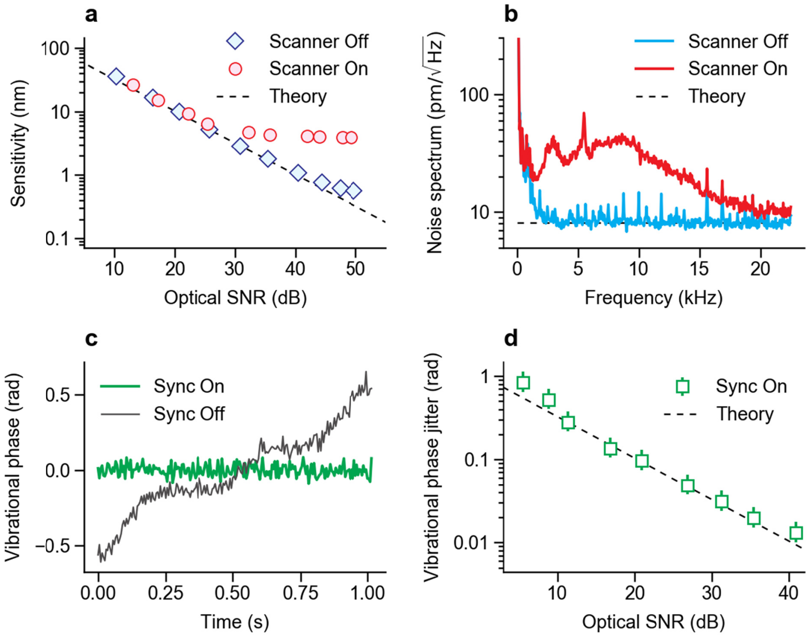

Fig. 3. Measured SNR and sensitivity. (a) The noise-equivalent displacement measured as a function of the SNR when the 2-axis galvanometer scanner was powered ON (red circles) or OFF (cyan circles), in comparison to the SNR-limited theoretical curve (dashed line). (b) Power spectra of the vibrational signal at a SNR of 35dB, when the scanner was powered off or on. (c) Measured vibration phases of the piezoelectric transducer showing the elimination of phase drift by synchronizing the phase of the stimulus signal to the acquisition board. (d) The standard deviation of the vibrational phase measured as a function of the SNR, which agrees well with the theoretical prediction (dashed line). Error bars represent 99% confidence intervals.

3. Results of chinchilla ear measurements

3.1 Vibrography imaging of the chinchilla middle ear

Vibrography experiments were performed on two cadaver chinchilla heads less than 2 weeks after sacrifice of animals. The specimens were kept frozen, and thawed a day before experiments. The head was mounted on a brass rod held in a multi-axis micro-positioner. The pinna, cartilaginous ear canal and much of the boney ear canal were removed to expose the central and superior areas of the TM. The thin dermal outer layer of the TM was removed to increase the transparency of the TM, and because the freeze thaw cycle had already loosened this layer over part of the TM surface. Laser-Doppler measurements have demonstrated that removing this layer has little effect on TM or ossicular motion. The specimen was positioned with a slight tilt around the long axis of the head to better view the incus and stapes. During each experiment, the remnant auditory canal was sealed to the sound coupling chamber using silicone molding material [40].

Prior to vibrography measurements, we scanned the OCT probe beam over the entire TM to acquire a 3D anatomical image of the middle ear. A representative cross-section and 3D rendered image are shown in Figs. 4(a) and 4(b). A large part of the ossicular chain could be observed, including the manubrium of the malleus underneath the TM, the long process of the incus, the anterior crus of the stapes, and the anterior stapes footplate. The head of the malleus and body of the incus are not visible because they are located behind the thick ear canal bone. Figure 4(c)-(e) show the reflectivity and axial velocity magnitude and phase (φ) maps of the cross-sectional plane, and clearly show all 3 ossicles: malleus, incus, and stapes. A 3 × 3 × 3 Gaussian filter was applied to the reflectivity and vibrometry maps to reduce speckle noise (Fig. 4(c)-(e)). The velocity and phase data were encoded in the structural image with color in a Hue-Saturation-Value (HSV) scheme using hue corresponding to the velocity or phase and color value being proportional to the reflectivity in log scale. The velocity was normalized to the sound pressure near the TM (in Pa) measured in real time using the microphone. The illustrated vibration phase is relative to the vibration of the umbo (rather than the speaker) so the phase at the umbo is always 0. The in-phase movement of much of the TM and three ossicles is clearly seen, whereas the vibration of the parts of the auditory canal and the wall and floor of the middle-ear cavity are of varied phase and of much smaller amplitude.

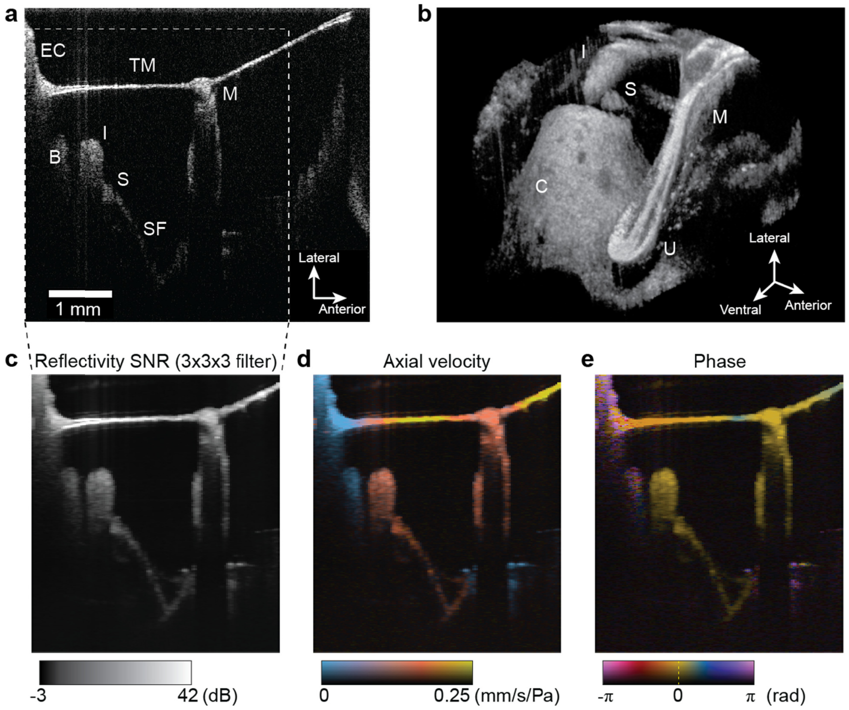

Fig. 4. OCT images of the chinchilla middle ear. (a) Representative cross-sectional image of a plane orthogonal to the manubrium (long handle of the malleus). (b) Orthographic 3D reconstruction with the TM digitally removed. (c-e) Cross-sectional vibrography images measured with SPL of 100 dB at 500 Hz after averaging over a 3x3x3 kernel of voxels. (c) standard reflectivity image in units of dB above the noise floor, (d) magnitude, and (e) phase maps. Labels: ear canal (EC), bone (B), manubrium (M), umbo (U), incus (I), stapes (S), stapes footplate (SF) and cochlear promontory (C).

3.2 Acoustic transfer function of the middle ear

To measure the acoustic transfer function of the middle ear, we used two different methods. First, we fixed the probe beam at the umbo and used a Schroeder frequency comb [41] to obtain the complete frequency response of the umbo over a frequency range of 100 Hz to 5 kHz. The broadband stimuli did not have sufficient acoustic power to produce sufficient SNR (> 10 dB) at frequencies above 5 kHz, although longer integration time could increase SNR. It was repeated for the probe beam fixed at the incus tip to measure the acoustic transfer function near the head of the stapes. This method is commonly used in conventional LDV measurements. The main difference is that the OCT measurement is performed through the intact TM, whereas LDV require the TM above the incus to be removed. The broadband results are presented as solid lines in Fig. 5(a).

In the second method, we acquired volumetric vibrography data at a specific monotonal sound stimulus and repeated the measurement for different sound frequencies, typically, at 0.36, 0.5, 1.0, 2.0, 3.0, 4.5, 6.4, 9.0, 11.3, and 15.0 kHz. The SPL was set to a range between 80 and 100 dB. The axial velocity and phase of the umbo, incus and stapes were obtained by manually selecting ROI's in the volumetric data set. The umbo ROI was defined as a 0.5mm diameter circle at the tip of the manubrium, and the incus and stapes ROI's were the entire visible portion of these ossicles. The data are shown in Fig. 5(a)-(c) as circle, triangle and square markers, respectively. The data obtained with the two distinct stimuli up to 5 kHz are in good agreement with each other. From 5 to 15 kHz, only results from monotonal stimulation are shown.

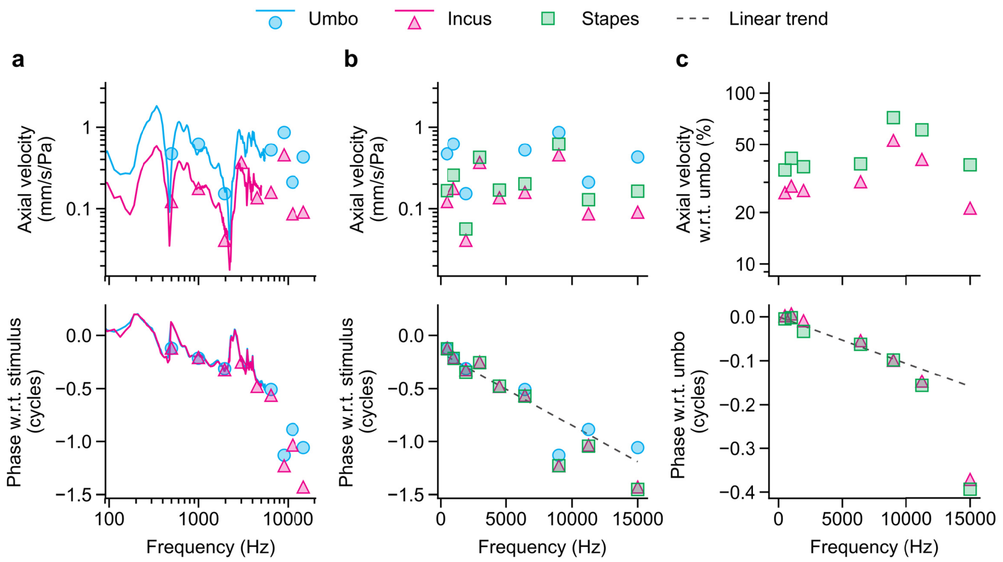

Fig. 5. Acoustic transfer function of the ossicular chain. (**a**) The axial velocity magnitude and phase φ at the umbo and incus as a function of sound frequency (log scale). Lines: data obtained with broadband sound stimulus; markers: data obtained at discrete frequencies. (b) The data of the umbo (cyan), incus (magenta), and stapes (green) over frequency (linear scale). (c) The axial velocity and phase of the incus and stapes with respect to the umbo.

From the volumetric data set, the acoustic transfer function at any location can be obtained. Figure 5(b) plots the velocity and phase transfer function of the stapes together with the data from the umbo and incus (in linear frequency scale). The phase of the umbo with respect to the sound stimulus varies with the frequency. A linear frequency dependence arises simply from wave propagation delay ($\partial\varphi/\partial f_a = 2\pi \times$ group delay time) [42]. The observed linear slope (dashed line) corresponds to an average delay time of ~67 µs. The distance of ~5 mm between the microphone and the TM accounts for 15 µs (sound speed: 340 m/s); the rest of the delay may be attributed to the phase delay in the acoustic coupling from air to the TM, and from the TM to the manubrium [42,43]. Figure 5(c) highlights the magnitude and phase of incus and stapes motion relative to that of the umbo. The vibration amplitude of the stapes (green squares) is larger than that of the incus (magenta triangles), but both move less (35-75%) than the umbo over the entire frequency range. As frequency increases, the phase of the incus and stapes deviate from that of the umbo. The negative phase slope in c indicates an additional delay in the motion of the stapes and incus relative to the umbo. At frequencies less than ~8 kHz, the phase follows a nearly linear trend (dashed line), indicating a simple group delay of the mechanical wave. Above that frequency there is a sudden increase in the phase difference between the umbo and the other two ossicles; as will be described later, this increase can be explained by the onset of a new mode of ossicular motion. These measurements of the relative sound-induced motion of the umbo, incus and stapes are consistent with past measurements in the same species performed using Mössbauer and LDV [5,9].

3.3 Projected and volumetric vibrography images of the TM and ossicular chain

Figure 6 show vibrography images of the TM in a top projection view at three different sound frequencies: 360 Hz, 4.5 kHz, and 9.0 kHz. At 360 Hz, the surface of the TM moves in phase with the stimulus. With increasing sound frequencies, the TM exhibits more complex vibration patterns with increasing numbers of maxima and minima in the velocity maps. The phase maps show complex patterns mixed with π phase shifts over a small distance, indicating standing waves, and more gradual phase gradients, indicating traveling waves. The presence of both standing and traveling components are consistent with previous measurements of sound-induced motion of the chinchilla TM using laser holography [40].

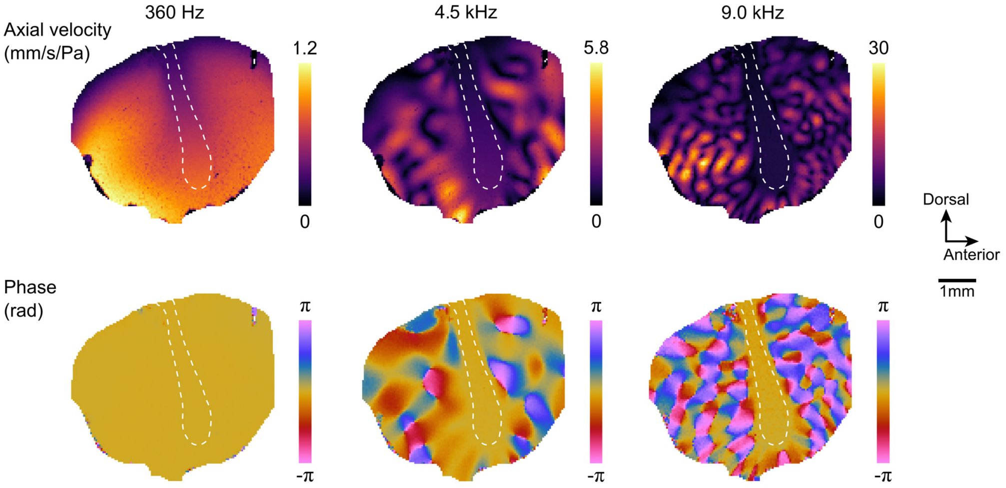

Fig. 6. Projection view of the TM vibration at 360 Hz (107 dB SPL), 4.5 kHz (100 dB SPL) and 9.0 kHz (84 dB SPL). The dotted lines show the outline of the manubrium. The phases are scaled relative to the phase of motion of the umbo.

Figure 7 shows constructed vibrography maps of the ossicular chain in a projection view at 500 Hz, 6.4 kHz, and 15.0 kHz. The most prominent structure is the manubrium of the malleus (M), and to its left, the inferior part of the long process of the incus (I) and the stapes (S) are seen. The head of the malleus and the body of the incus are behind the ear canal bone and so are not visible. At 500 Hz, the axial velocity increases along the manubrium from the lateral process (LP) to the umbo (U) (Fig. 7(a)), and the ossicles move all in phase (Fig. 7(d)). This motion is consistent with a lever-like rotation around the malleus-incus joint. At higher frequencies, the velocity gradient along the manubrium is increasingly nonlinear (Fig. 7(b) and 7(c)), and the phase of the upper most portion of the malleus (the lateral process), incus, and stapes lag from that of the umbo (Fig. 7(e) and 7(f)).

Phase gradients along the manubrium can be appreciated more easily with a reduced phase range for the color-coded display, shown in Fig. 7(g)-(i). At 6.4 kHz, the phase gradient along the manubrium indicates a flexural motion of the ossicle (Fig. 7(h)). At 15 kHz, while the axial flex is present, most interestingly, a lateral phase gradient appears (Fig. 7(i)), suggesting a twist motion around the axis.

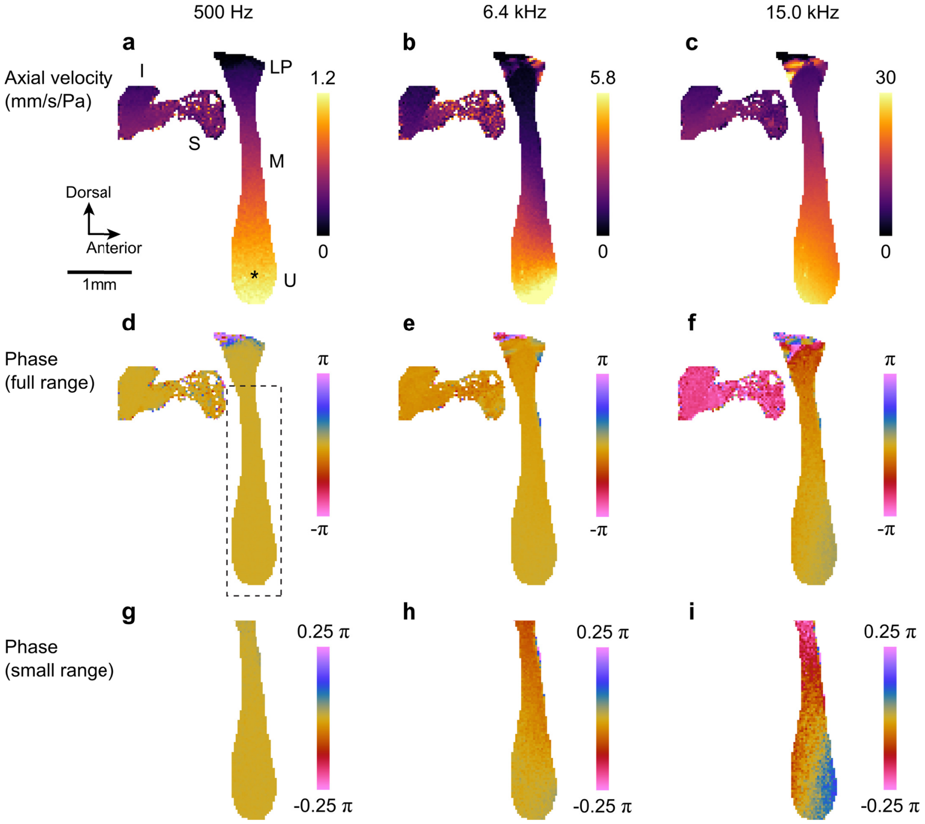

Fig. 7. Projection view of the ossicular chain at 500 Hz (100 dB SPL), 6.4 kHz (108 dB SPL), and 15 kHz (103 dB SPL). (a-c) Axial velocity maps. (d-e) Phase maps relative to the umbo. (g-i) Phase maps of the manubrium (dashed box in d) relative to the umbo. The range of the colormap is reduced to help visualize phase gradients along the manubrium. Labels: manubrium (M), incus (I), stapes (S), lateral process (LP), umbo (U); * shows the umbo location used as phase reference.

From the volumetric data set, we constructed 3-dimensional rendering of the ossicular motion with exaggerated vibration amplitude. The movies taken at 500 Hz and 15 kHz clearly show the differences in the ossicular motion, particularly of the manubrium (Fig. 8(a)). At the low frequency, the in-phase rotational motion of the manubrium, incus and stapes around the malleus-incus axis is predominant. At 15 kHz, this fundamental rotational mode is accompanied by the second rotational motion around a new axis parallel to the manubrium. In addition, the twist motion and flexural bending of the manubrium are noticeable. Figure 8b illustrates the two modes of ossicular motion.

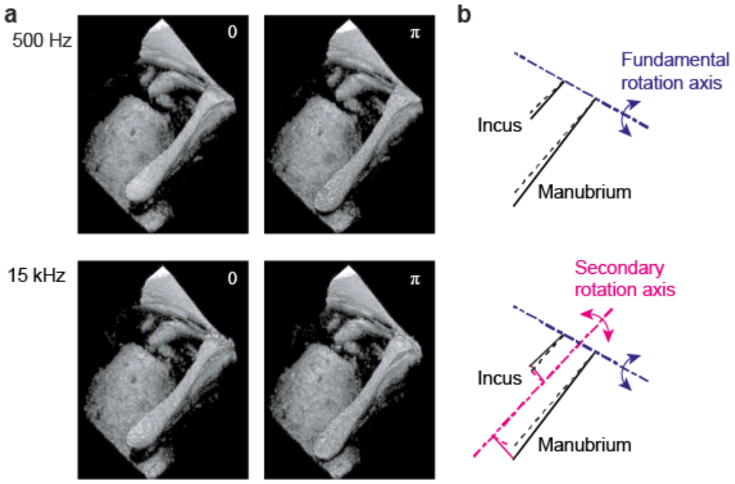

Fig. 8. Reconstructed ossicular motion at 500 Hz and 15.0 kHz. (a) Motion-exaggerated animations and representative snapshots at φ = 0 and π. See Supplementary Visualization 1 for 500 Hz and Supplementary Visualization 2 for 15 kHz. (b) Schematics of the two rotational modes of ossicular motion. The fundamental mode is predominant at frequencies below 5 kHz. Above 9 kHz, the secondary rotational motion becomes evident.

4. Discussion

The acoustic transfer function, projection phase maps, and reconstructed 3D rendered animations provide comprehensive and quantitative information and clear insights about the sound-driven motion of the ossicular chain. The near-half-cycle difference between the umbo and the incus-stapes at 15 kHz is consistent with the second ossicular rotational axis that is parallel to the manubrium and positioned between the manubrium and the incus. Such rotational modes have been hypothesized for small mammals by Fleischer [44]. This additional rotational mode of the ossicular chain can function to increase the motion of the incus and stapes at higher frequencies and may contribute critically to the efficient acoustic conduction of the ossicular chain over 10 octaves of sound frequency [45].

OCT shows promise as a tool to aid the diagnosis of middle ear pathology, by allowing visualization of middle-ear structure behind the TM, and quantification of sound-induced ossicular motion that can help distinguish abnormal function and its causes [31]. The maximum sound frequency in the current OCT system is limited to the Nyquist frequency of 22.5 kHz. This frequency range is adequate for hearing research in humans (20 Hz to 20 kHz hearing range), and covers most of the chinchilla hearing range (50 Hz to 33 kHz) [46]. The total duration of a volumetric measurement, on the order of a minute, is a challenge for live patient or animal imaging due to motion artifacts. One possible approach, explored by MacDougall and colleagues [29], is to use standard anatomic OCT imaging to target a single location at which vibrometry can rapidly be performed. OCT systems with higher A-line rates of up to several MHz have been reported [47,48] and may enable considerable reduction of the total measurement time by allowing data acquisition in the B-M mode (comparing phases between successive B-scans [49]) instead of the M-B mode (comparing phases between successive A-lines) used in this study.

In conclusion, we have described OCT vibrography for measuring and visualizing the sound-induced motion of the ossicles and TM and demonstrated its usefulness through the measurement of the chinchilla ear. The acoustic transfer functions we recorded are consistent with previous measurements obtained by LDVs and holography measurements. However, the unique ability of OCT vibrography to acquire volumetric data in conjunction with 3D structural images enabled us to appreciate the greater details of the ossicular motion, including the fundamental rotation around the malleus-incus axis and, importantly, to identify a second rotational mode of ossicular motion at high frequencies. Our results demonstrate OCT vibrography as a powerful tool in hearing research.

Funding

National Institutes of Health (P41-EB015903, R01-DC000194); Fonds de Recherche du Québec.

Acknowledgements

We thank Brian Battersby for his help with software development.

Disclosures

The authors declare that there are no conflicts of interest related to this article.

References and links

1. A. M. Huber, C. Schwab, T. Linder, S. J. Stoeckli, M. Ferrazzini, N. Dillier, and U. Fisch, “Evaluation of eardrum laser doppler interferometry as a diagnostic tool,” Laryngoscope **111**(3), 501–507 (2001).
2. J. J. Rosowski, H. H. Nakajima, and S. N. Merchant, “Clinical utility of laser-Doppler vibrometer measurements in live normal and pathologic human ears,” Ear Hear. **29**(1), 3–19 (2008).
3. T. Zahnert, M.-L. Metasch, H. Seidler, M. Bornitz, N. Lasurashvili, and M. Neudert, “A new intraoperative real-time monitoring system for reconstructive middle ear surgery: an experimental and clinical feasibility study,” Otol. Neurotol. **37**(10), 1601–1607 (2016).
4. G. von Békésy, “Über die Messung Schwingungsamplitude der Gehörknochelchen mittels einer kapazitiven Sonde [About the vibration amplitude of the ossicles measured by means of a capacitive probe],” Akust Zeits **6**, 1–16 (1941).
5. M. A. Ruggero, N. C. Rich, L. Robles, and B. G. Shivapuja, “Middle-ear response in the chinchilla and its relationship to mechanics at the base of the cochlea,” J. Acoust. Soc. Am. **87**(4), 1612–1629 (1990).
6. S. M. Khanna and J. Tonndorf, “Tympanic Membrane Vibrations in Cats Studied by Time-Averaged Holography,” J. Acoust. Soc. Am. **51**(6), 1904–1920 (1972).
7. J. Tonndorf and S. M. Khanna, “Submicroscopic displacement amplitudes of the tympanic membrane (cat) measured by a laser interferometer,” J. Acoust. Soc. Am. **44**(6), 1546–1554 (1968).
8. P. Razavi, M. E. Ravicz, I. Dobrev, J. T. Cheng, C. Furlong, and J. J. Rosowski, “Response of the human tympanic membrane to transient acoustic and mechanical stimuli: Preliminary results,” Hear. Res. **340**, 15–24 (2016).
9. L. Robles, A. N. Temchin, Y.-H. Fan, and M. A. Ruggero, “Stapes Vibration in the Chinchilla Middle Ear: Relation to Behavioral and Auditory-Nerve Thresholds,” J. Assoc. Res. Otolaryngol. **16**(4), 447–457 (2015).
10. O. de La Rochefoucauld, S. M. Khanna, and E. S. Olson, “Recording depth and signal competition in heterodyne interferometry,” J. Acoust. Soc. Am. **117**(3), 1267–1284 (2005).
11. C. Pitris, K. T. Saunders, J. G. Fujimoto, and M. E. Brezinski, “High-Resolution Imaging of the Middle Ear with Optical Coherence Tomography: A Feasibility Study,” Arch. Otolaryngol. Head Neck Surg. **127**(6), 637–642 (2001).
12. G. L. Monroy, R. L. Shelton, R. M. Nolan, C. T. Nguyen, M. A. Novak, M. C. Hill, D. T. McCormick, and S. A. Boppart, “Noninvasive depth-resolved optical measurements of the tympanic membrane and middle ear for differentiating otitis media,” Laryngoscope **125**(8), E276–E282 (2015).
13. G. L. Monroy, P. Pande, R. L. Shelton, R. M. Nolan, D. R. Spillman, Jr., R. G. Porter, M. A. Novak, and S. A. Boppart, “Non-invasive optical assessment of viscosity of middle ear effusions in otitis media,” J. Biophotonics **10**(3), 394–403 (2017).
14. H. R. Djalilian, M. Rubinstein, E. C. Wu, K. Naemi, S. Zardouz, K. Karimi, and B. J. F. Wong, “Optical Coherence Tomography of Cholesteatoma,” Otol. Neurotol. **31**(6), 932–935 (2010).
15. R. Heermann, C. Hauger, P. R. Issing, and T. Lenarz, “Application of Optical Coherence Tomography (OCT) in middle ear surgery,” Laryngorhinootologie **81**(6), 400–405 (2002).
16. T. Just, E. Lankenau, G. Hüttmann, and H. W. Pau, “Optical coherence tomography of the oval window niche,” J. Laryngol. Otol. **123**(6), 603–608 (2009).
17. H. Y. Lee, P. D. Raphael, J. Park, A. K. Ellerbee, B. E. Applegate, and J. S. Oghalai, “Noninvasive in vivo imaging reveals differences between tectorial membrane and basilar membrane traveling waves in the mouse cochlea,” Proc. Natl. Acad. Sci. U.S.A. **112**(10), 3128–3133 (2015).
18. N. Choudhury, G. Song, F. Chen, S. Matthews, T. Tschinkel, J. Zheng, S. L. Jacques, and A. L. Nuttall, “Low coherence interferometry of the cochlear partition,” Hear. Res. **220**(1-2), 1–9 (2006).
19. S. Page, R. Ghaffari, and D. M. Freeman, “Doppler optical coherence microscopy and tomography applied to inner ear mechanics,” in *AIP Conf. Proc. Mechanics of Hearing: Protein to Perception* (2015), **040002**, 040002.
20. T. Ren, W. He, and P. G. Barr-Gillespie, “Reverse transduction measured in the living cochlea by low-coherence heterodyne interferometry,” Nat. Commun. **7**, 10282 (2016).
21. A. Recio-Spinoso and J. S. Oghalai, “Mechanical tuning and amplification within the apex of the guinea pig

cochlea," J. Physiol. **595**(13), 4549–4561 (2017).
22. R. L. Warren, S. Ramamoorthy, N. Ciganović, Y. Zhang, T. M. Wilson, T. Petrie, R. K. Wang, S. L. Jacques, T. Reichenbach, A. L. Nuttall, and A. Fridberger, "Minimal basilar membrane motion in low-frequency hearing," Proc. Natl. Acad. Sci. U.S.A. **113**(30), E4304–E4310 (2016).
23. R. K. Wang and A. L. Nuttall, "Phase-sensitive optical coherence tomography imaging of the tissue motion within the organ of Corti at a subnanometer scale: a preliminary study," J. Biomed. Opt. **15**(5), 056005 (2010).
24. H. M. Subhash, A. Nguyen-Huynh, R. K. Wang, S. L. Jacques, N. Choudhury, and A. L. Nuttall, "Feasibility of spectral-domain phase-sensitive optical coherence tomography for middle ear vibrometry," J. Biomed. Opt. **17**(6), 060505 (2012).
25. A. Burkhardt, L. Kirsten, M. Bornitz, T. Zahnert, and E. Koch, "Investigation of the human tympanic membrane oscillation ex vivo by Doppler optical coherence tomography," J. Biophotonics **7**(6), 434–441 (2014).
26. J. Park, E. F. Carbajal, X. Chen, J. S. Oghalai, and B. E. Applegate, "Phase-sensitive optical coherence tomography using an Vernier-tuned distributed Bragg reflector swept laser in the mouse middle ear," **39**, Opt. Lett. 6233 (2014).
27. L. Kirsten, S. Baumgärtner, M. T. Erkkilä, J. Golde, M. Kemper, T. Stoppe, M. Bornitz, M. Neudert, T. Zahnert, and E. Koch, "Doppler optical coherence tomography as a promising tool for detecting fluid in the human middle ear," Curr. Dir. Biomed. Eng. **2**, 443–447 (2016).
28. S. Choi, K. Sato, T. Ota, F. Nin, S. Muramatsu, and H. Hibino, "Multifrequency-swept optical coherence microscopy for highspeed full-field tomographic vibrometry in biological tissues," Biomed. Opt. Express **8**(2), 608–621 (2017).
29. D. MacDougall, J. Farrell, J. Brown, M. Bance, and R. Adamson, "Long-range, wide-field swept-source optical coherence tomography with GPU accelerated digital lock-in Doppler vibrography for real-time, *in vivo* middle ear diagnostics," Biomed. Opt. Express **7**(11), 4621–4635 (2016).
30. J. Park, J. T. Cheng, D. Ferguson, G. Maguluri, E. W. Chang, C. Clancy, D. J. Lee, and N. Iftimia, "Investigation of middle ear anatomy and function with combined video otoscopy-phase sensitive OCT," Biomed. Opt. Express **7**(2), 238–250 (2016).
31. E. W. Chang, J. T. Cheng, C. Röösli, J. B. Kobler, J. J. Rosowski, and S. H. Yun, "Simultaneous 3D imaging of sound-induced motions of the tympanic membrane and middle ear ossicles," Hear. Res. **304**, 49–56 (2013).
32. S. Yun, G. Tearney, J. de Boer, N. Iftimia, and B. Bouma, "High-speed optical frequency-domain imaging," Opt. Express **11**(22), 2953–2963 (2003).
33. S. H. Yun, G. J. Tearney, B. J. Vakoc, M. Shishkov, W. Y. Oh, A. E. Desjardins, M. J. Suter, R. C. Chan, J. A. Evans, I.-K. Jang, N. S. Nishioka, J. F. de Boer, and B. E. Bouma, "Comprehensive volumetric optical microscopy in vivo," Nat. Med. **12**(12), 1429–1433 (2006).
34. E. W. Chang, J. B. Kobler, and S. H. Yun, "Subnanometer optical coherence tomographic vibrography," Opt. Lett. **37**(17), 3678–3680 (2012).
35. B. Braaf, K. A. Vermeer, V. A. D. P. Sicam, E. van Zeeburg, J. C. van Meurs, and J. F. de Boer, "Phase-stabilized optical frequency domain imaging at 1-µm for the measurement of blood flow in the human choroid," Opt. Express **19**(21), 20886–20903 (2011).
36. B. Vakoc, S. Yun, J. de Boer, G. Tearney, and B. Bouma, "Phase-resolved optical frequency domain imaging," Opt. Express **13**(14), 5483–5493 (2005).
37. C. Kasai, K. Namekawa, A. Koyano, and R. Omoto, "Real-time two-dimensional blood flow imaging using an autocorrelation technique," IEEE Trans. Sonics Ultrason. **32**(3), 458–464 (1985).
38. M. A. Choma, A. K. Ellerbee, C. Yang, T. L. Creazzo, and J. A. Izatt, "Spectral-domain phase microscopy," Opt. Lett. **30**(10), 1162–1164 (2005).
39. S. Yazdanfar, C. Yang, M. Sarunic, and J. Izatt, "Frequency estimation precision in Doppler optical coherence tomography using the Cramer-Rao lower bound," Opt. Express **13**(2), 410–416 (2005).
40. J. J. Rosowski, I. Dobrev, M. Khaleghi, W. Lu, J. T. Cheng, E. Harrington, and C. Furlong, "Measurements of three-dimensional shape and sound-induced motion of the chinchilla tympanic membrane," Hear. Res. **301**, 44–52 (2013).
41. M. Schroeder, "Synthesis of low-peak-factor signals and binary sequences with low autocorrelation (Corresp.)," IEEE Trans. Inf. Theory **16**(1), 85–89 (1970).
42. M. E. Ravicz and J. J. Rosowski, "Middle-ear velocity transfer function, cochlear input immittance, and middle-ear efficiency in chinchilla," J. Acoust. Soc. Am. **134**(4), 2852–2865 (2013).
43. S. Puria and J. B. Allen, "Measurements and model of the cat middle ear: evidence of tympanic membrane acoustic delay," J. Acoust. Soc. Am. **104**(6), 3463–3481 (1998).
44. G. Fleischer, "Evolutionary principles of the mammalian middle ear," Adv. Anat. Embryol. Cell Biol. **55**(5), 3–70 (1978).
45. S. Puria and C. Steele, "Tympanic-membrane and malleus-incus-complex co-adaptations for high-frequency hearing in mammals," Hear. Res. **263**(1-2), 183–190 (2010).
46. R. S. Heffner and H. E. Heffner, "Behavioral hearing range of the chinchilla," Hear. Res. **52**(1), 13–16 (1991).
47. T. Klein and R. Huber, "High-speed OCT light sources and systems [Invited]," Biomed. Opt. Express **8**(2), 828–859 (2017).
48. M. Siddiqui, A. S. Nam, S. Tozburun, N. Lippok, C. Blatter, and B. J. Vakoc, "High-speed optical coherence tomography by circular interferometric ranging," Nat. Photonics **12**(2), 111–116 (2018).
49. S. Song, W. Wei, B.-Y. Hsieh, I. Pelivanov, T. T. Shen, M. O'Donnell, and R. K. Wang, "Strategies to improve

phase-stability of ultrafast swept source optical coherence tomography for single shot imaging of transient mechanical waves at 16 kHz frame rate," Appl. Phys. Lett. **108**(19), 191104 (2016).